

Representing arbitrary ground states of the toric code by a restricted Boltzmann machine

Penghua Chen², Bowen Yan², and Shawn X. Cui ^{*1,2}

¹Department of Mathematics, Purdue University, West Lafayette

²Department of Physics and Astronomy, Purdue University, West Lafayette

{chen3014, yan312, cui177} @purdue.edu

Abstract

We systematically analyze the representability of toric code ground states by Restricted Boltzmann Machine with only local connections between hidden and visible neurons. This analysis is pivotal for evaluating the model's capability to represent diverse ground states, thus enhancing our understanding of its strengths and weaknesses. Subsequently, we modify the Restricted Boltzmann Machine to accommodate arbitrary ground states by introducing essential non-local connections efficiently. The new model is not only analytically solvable but also demonstrates efficient and accurate performance when solved using machine learning techniques. Then we generalize our the model from Z_2 to Z_n toric code and discuss future directions.

1 Introduction

The research on topological phases of matter (TPMs) has significantly intensified in recent decades. These phases are characterized by topological order, setting them apart from conventional states. Topological phases feature ground states with stable degeneracy and robust long-range entanglement. In two dimensions, they support anyons and show resilience to local disruptions. These unique attributes render TPMs highly suitable for fault-tolerant quantum computing [1, 2]. In two dimensions, the underlying structure of TPMs can be described by either a (2+1)-dimensional topological quantum field theory or a unitary modular tensor category. Many topological phases can be realized on spin lattice models, with the toric code model standing out as one of the most notable examples. More generally, associated with each finite group G , Kitaev's quantum double model defines an exactly solvable lattice model realizing possibly non-Abelian anyons. When $G = \mathbb{Z}_2$, the theory simplifies to the toric code.

Identifying the eigenstates of the Hamiltonian of a topological phase, and more generally that of a many-body quantum system, ranks among the most demanding tasks in condensed matter physics. This task becomes increasingly complex primarily because of

^{*}Corresponding author

the power scaling of the Hilbert space dimension, which inflates exponentially in relation to the system's size [3]. Nonetheless, it is often the case that the system's inherent physical properties, e.g. long-range entanglement, restrict the form of the ground states, and therefore the states corresponding to interesting quantum systems may only occupy a small portion of the exponentially large Hilbert space. This opens up the possibility of efficient representations of the wave function of many-body systems. Examples of efficient representations include matrix product states, projected entangled pair states, and more generally tensor networks.

A recent trend is the study of many-body quantum systems utilizing machine learning techniques, especially artificial neural networks. Restricted Boltzmann Machines (RBMs) are a generative stochastic artificial neural network [4]. Unlike other types of neural networks, RBMs have a unique two-layer architecture that consists of a visible input layer and a hidden layer. The 'restricted' part in the name refers to the lack of intra-layer connections; that is, nodes within the same layer do not interact with each other. RBMs have been used effectively in a variety of machine learning tasks, including dimensionality reduction, classification, regression, and even solving quantum many-body problems [5, 6, 7, 8, 9, 10, 11].

In 2017, Carleo and Troyer paved a novel path by applying RBM as a variational ansatz, utilizing it to represent ground states for Ising model [5]. This groundbreaking achievement catalyzed the development of numerous explicit RBM representations. Notably, substantial research efforts have been directed towards the examination of toric code [6, 7], tensor network state[8], graph states [9], and stabilizer code [10, 11], which is equivalent to a graph state under local Clifford operations [12]. While their topological properties and representational power [13, 14] have been extensively studied, there is still a need to explore feasible algorithms for specific models.

We start from the RBM representability of the toric code model as the first step, with the eventual goal of studying that for general topological phases. In [7], the authors utilized a Further Restricted Restricted Boltzmann Machine (FRRBM), that allows only local connections, to numerically find a ground state solution¹ of the toric code model. However, toric code has degeneracy on non-trivial topology, and the ground state derived in the above manner always corresponds certain specific one. In contrast, [8] presented an alternative approach, deriving a four-fold degenerate basis of ground states that can be understood by applying logical operators on the 'trivial solution'² solved from the FRRBM. On the other hand, it is possible to achieve an arbitrary ground state by turning the toric code as a graph state [15] and transforming a graph state into an RBM [10]. Yet, this approach inevitably introduces non-local connections within each subgraph which adds to the complexity of the RBM.

In this work, we initially apply stabilizer conditions to several specific configurations to analytically solve the FRRBM for the toric code, exploring its representational capacity. We factorize these ground state solutions on square lattices of various sizes and find that different weights only alter the coefficients of the basis states forming the ground state by factors of ± 1 . We then extended this approach to obtain an arbitrary ground state by strategically introducing several non-local connections into the RBM. While this generalization sacrifices the simplicity of local connections, it remains analytically solvable, enabling the simulation of arbitrary ground states in a clean manner. Additionally,

¹Throughout the text, we use the term "solution" primarily to refer to the set of parameters obtained by solving the conditions that ensure the RBM represents a ground state.

²This is the simplest solution solved in Section 5 and further generalized in Section 8.

we develop an efficient machine learning algorithm to verify the learnability of the models. We further generalize our approach from Z_2 to Z_n and outline potential directions for future research.

2 Toric code

The toric code represents the most elementary example of Kitaev’s quantum double models where $G = \mathbb{Z}_2$. It is defined on a square lattice, topologically equivalent to a torus as shown in Figure 1. A spin $1/2$ is located on each edge e of the lattice, and we also use e to denote the associated qubit. The lattice components—vertices, faces, and edges—are denoted as V , F , and E , respectively. For each face $f \in F$, the set of surrounding edges is denoted by $s(f)$, and similarly, for each vertex $v \in V$, the set of surrounding edges is $s(v)$. The vertex operator A_v consists of tensor products of Pauli operators $\hat{\sigma}_e^x$ acting on the edges e within $s(v)$. Similarly, the face operator B_f is formed from tensor products of Pauli operators $\hat{\sigma}_e^z$ acting on the edges e within $s(f)$. The Hamiltonian of the toric code is defined as the sum of all vertex and face operators:

$$H = - \sum_{v \in V} A_v - \sum_{f \in F} B_f = - \sum_{v \in V} \prod_{e \in s(v)} \hat{\sigma}_e^x - \sum_{f \in F} \prod_{e \in s(f)} \hat{\sigma}_e^z. \quad (1)$$

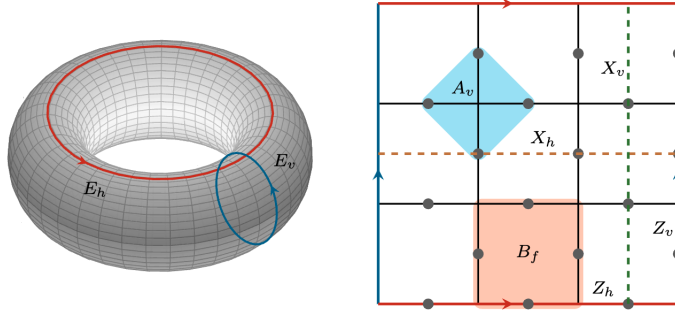


Figure 1: The torus on the left is cut along the edges E_v and E_h to get the square lattice shown on the right, with opposite edges identified. The 3×3 lattice shows stabilizer operators A_v within the blue range and B_f within the red range, logical operators X_v and X_h along the vertical and horizontal dashed loops, respectively, and logical operators Z_v and Z_h along the edges E_v and E_h .

For a Hamiltonian of the form

$$H = - \sum_i P_i, \quad (2)$$

where each P_i is a projector and all projectors are mutually commuting, the ground state $|GS\rangle$ can be derived from any arbitrary non-zero state $|\phi\rangle$:

$$|GS\rangle = \prod_i P_i |\phi\rangle. \quad (3)$$

This construction ensures that the ground state is the simultaneous eigenvector of all projectors. Given $A_v^2 = B_f^2 = 1$ and $[A_v, B_f] = 0$ for all $v \in V$ and $f \in F$, it can be

confirmed that $\frac{1+A_v}{2}$ and $\frac{1+B_f}{2}$ act as projectors. Replacing A_v and B_f in the Hamiltonian with these projectors yields a equivalent form consistent with Equation 2. This equivalence, stemming from a one-to-one correspondence in their spectra, ensures that the state

$$|GS\rangle = \prod_{v \in V} \frac{1+A_v}{2} \prod_{f \in F} \frac{1+B_f}{2} |\phi\rangle \quad (4)$$

is a valid ground state as per the earlier defined criteria. Notice that the toric code model is inherently a stabilizer code, with the local Hamiltonian terms A_v and B_f acting as stabilizer operators. In the context of error-correcting codes, the ground states function as logical states. The operators that dissolve these ground states are known as logical operators³. As described in [1], the degeneracy of the ground states for a 2D toric code on a torus is identified as four distinct states: $|00\rangle$, $|01\rangle$, $|10\rangle$, and $|11\rangle$. The logical operators X_v and X_h consist of strings of $\hat{\sigma}_e^x$ acting along the vertical and horizontal loops, respectively, transforming $|00\rangle$ to $|01\rangle$ and $|10\rangle$. Similarly, the logical operators Z_v and Z_h consist of strings of $\hat{\sigma}_e^z$ acting along E_v and E_h , respectively, distinguish $|00\rangle$ from $|01\rangle$ and $|10\rangle$.

3 Restricted Boltamann Machines

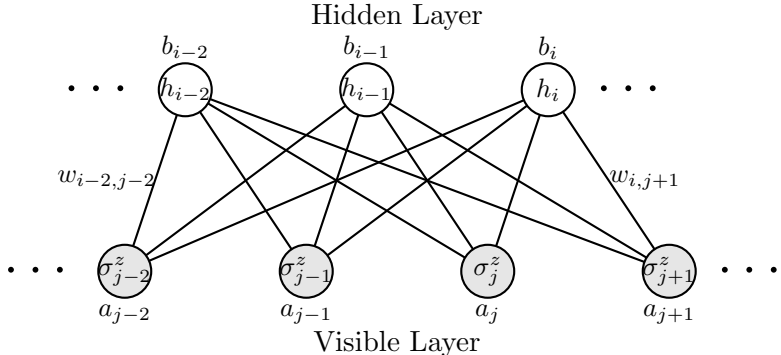


Figure 2: This diagram illustrates a RBM with visible neurons colored gray and hidden neurons colored white. The architecture ensures there are no intra-layer connections; instead, each hidden neuron is connected to all visible neurons. Each neuron and each connection is assigned a weight.

In the literature [5], Carleo and Troyer employ an Restricted Boltamann Machines (RBM) as a variational ansatz for the spin-half Ising model, as illustrated in Figure 2. The neural network consists of a layer of visible neurons corresponding to N physical spins in the configuration $S = (\sigma_1^z, \sigma_2^z, \dots, \sigma_N^z)$ ⁴, and a single hidden layer containing M auxiliary spins represented as $M = (h_1, h_2, \dots, h_M)$. The wave function for the configuration is expressed in the variational form:

$$\Psi_M(S; \mathcal{W}) = \sum_{\{h_i\}} e^{\sum_j a_j \sigma_j^z + \sum_i b_i h_i + \sum_{ij} h_i w_{ij} \sigma_j^z}, \quad (5)$$

³ Z_h and X_v , as well as Z_v and X_h , serve as pairs of logical X and Z operators for the two logical qubits, and are thus named as the logical operators.

⁴Throughout this paper, we use $\hat{\sigma}^z$ for operators and use σ^z for classical variables, $\sigma^z = \pm 1$.

where $\{h_i\} = \{-1, 1\}^M$ represents all possible configurations of the hidden auxiliary spins. The network weights $\mathcal{W} = (a_i, b_j, w_{i,j})$ can then be trained to optimize

$$|\Psi\rangle = \sum_S \Psi_M(S; \mathcal{W}) |S\rangle \quad (6)$$

to best represent the ground state $|GS\rangle$. As RBM restricts intralayer interactions, we may trace out all hidden variables according to the chosen preferred basis to simplify the wave function:

$$\Psi_M(S; \mathcal{W}) = e^{\sum_j a_j \sigma_j^z} \prod_i 2 \cosh(b_i + \sum_j w_{i,j} \sigma_j^z). \quad (7)$$

4 Further Restricted RBM

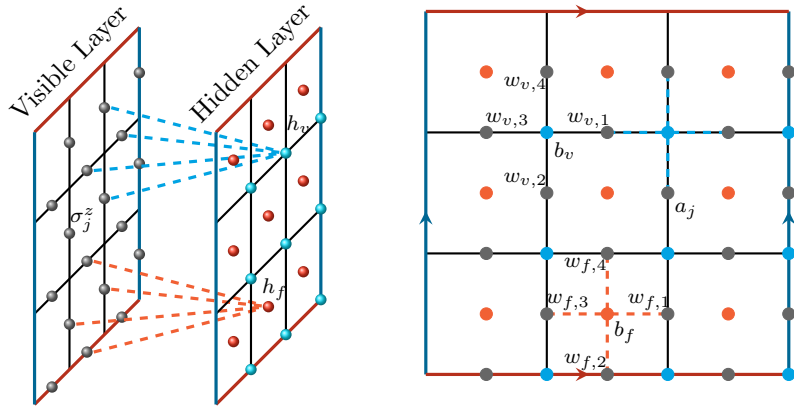


Figure 3: The right diagram results from collapsing the two layers shown in the left diagram. It illustrates a translation-invariant FRRBM with visible neurons colored gray and hidden neurons colored red and blue, corresponding to faces and vertices, respectively. The architecture ensures that each hidden neuron is connected only to the nearest visible neurons. Each neuron and each connection is assigned a weight.

To simulate the ground state of the 2D toric code, the authors in [7] utilized a translation-invariant Further Restricted RBM (FRRBM), illustrated in Figure 3. This model, designed to permit only local connections, was employed to numerically find a ground state solution. For the physical spins $\{\sigma_j^z\}$ on the square lattice, a vertex-type hidden neuron h_v was assigned to each vertex and a face-type hidden neuron h_f to each face, with connections limited to the nearest visible neurons. Given the two types of hidden neurons, the wave function, as shown in Equation (7), is reformulated as follows:

$$\Psi_M(S; \mathcal{W}) = e^{\sum_j a_j \sigma_j^z} \prod_{v \in V} \Gamma_v(S; \mathcal{W}) \prod_{f \in F} \Gamma_f(S; \mathcal{W}), \quad (8)$$

$$\Gamma_v(S; \mathcal{W}) = 2 \cosh(b_v + \sum_{j \in s(v)} w_{v,j} \sigma_j^z), \quad (9)$$

$$\Gamma_f(S; \mathcal{W}) = 2 \cosh(b_f + \sum_{j \in s(f)} w_{f,j} \sigma_j^z). \quad (10)$$

They set weight $a_j = 0$ for every visible neuron, choose $(b_f, w_{f,j}) = (0, \frac{\pi}{4}i)$. Using the stabilizer conditions, they train the FRRBM to get the translational invariant and isotropic solution numerically, resulting in $(b_v, w_{v,j}) = (0, \frac{\pi}{2}i)$. This FRRBM also naturally supports excited states if translation-invariant symmetry is broken and string operators are applied. Furthermore, this solution can be directly generalized to the 3D toric code.

5 Analytical solutions to the FRRBM model

However, the solution derived above is limited to describing only one specific ground state. To fully explore the representational capacity of the FRRBM, we aim to analytically solve it to identify all possible ground state solutions. We begin with the translation-invariant wave function described above and also set $a_j = 0$ for every visible neuron. Then we solve $\mathcal{W} = (b_f, w_{f,1-4}, b_v, w_{v,1-4})$ using the stabilizer conditions:

$$B_f|GS\rangle = \prod_{e \in s(f)} \hat{\sigma}_e^z|GS\rangle = |GS\rangle, \forall f \in F; \quad (11)$$

$$A_v|GS\rangle = \prod_{e \in s(v)} \hat{\sigma}_e^x|GS\rangle = |GS\rangle, \forall v \in V. \quad (12)$$

Solving the face stabilizer condition is straightforward, as the operator $\hat{\sigma}_e^z$ does not alter the state of the qubit e . By substituting Equation (8) into Equation (6) and treating $|\Psi\rangle$ as the ground state $|GS\rangle$, we solve for $|\Psi\rangle$ under the constraints imposed by Equation (11). This process is applied within any single face to determine: $b_f = 0 \pmod{\pi}$ and $w_{f,j} = \frac{\pi}{4}i, \frac{3\pi}{4}i \pmod{\pi}$, where an even number of the four $w_{f,j}$ must be the same. Further calculation details are provided in Appendix A.

Unlike the face stabilizer condition, solving the vertex stabilizer condition is more complex. The operator $\hat{\sigma}_e^x$ flips the state of qubit e . As shown in Figure 4, applying vertex operator to any vertex $v_0 \in V$ alters the configuration from $|S\rangle$ to $|h_0(S)\rangle$. Notably, applying the vertex operator twice will restore the original configuration. Applying the constraints outlined in Equation (12), we derive the following result:

$$\sum_S \prod_{v \in V} \Gamma_v(S; \mathcal{W}) \prod_{f \in F} \Gamma_f(S; \mathcal{W}) |h_0(S)\rangle = \sum_S \prod_{v \in V} \Gamma_v(S; \mathcal{W}) \prod_{f \in F} \Gamma_f(S; \mathcal{W}) |S\rangle. \quad (13)$$

By applying it twice, we can remove the sum to get

$$\prod_{v \in V} \Gamma_v(h_0(S); \mathcal{W}) \prod_{f \in F} \Gamma_f(h_0(S); \mathcal{W}) = \prod_{v \in V} \Gamma_v(S; \mathcal{W}) \prod_{f \in F} \Gamma_f(S; \mathcal{W}) \quad (14)$$

for any possible configuration S . However, there are many equal factors on both sides of the Equation (14). Canceling out them will reduce the configuration of interest from S to S' which only contains 16 qubits, giving a series of 2^{16} equations. Directly solving these equations is impossible. We can pick up particular configurations and apply one or more vertex operators on it to get independent restrictions. Full calculation details are provided in Appendix B, solving them out, we get⁵: $b_v = 0 \pmod{\pi}$ and $w_{v,j} = 0, \frac{\pi}{2}i \pmod{\pi}$, where an even number of the four $w_{v,j}$ must be the same; Otherwise $b_v = 0 \pmod{\pi}$ and any three of the four $w_{v,j}$ are equal to 0 or $\frac{\pi}{2} \pmod{\pi}$ while the other one is free.

⁵We take $b_v = 0$ as $b_v \in \mathbb{C}$ will introduce superfluous freedom, discussed in Appendix B.

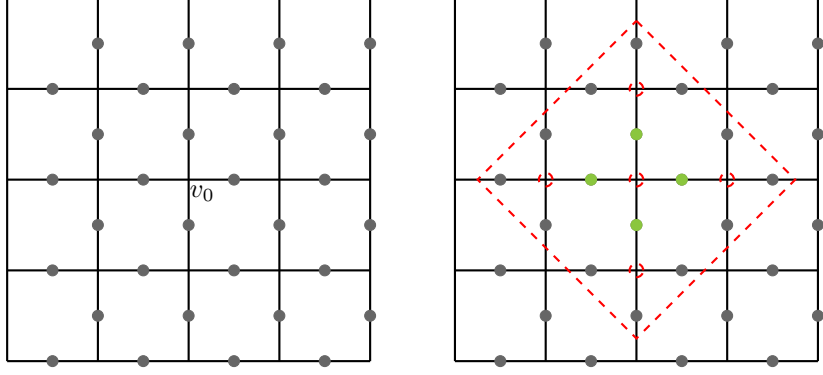


Figure 4: The left diagram presents a partial view of a configuration on a larger square lattice. The right diagram is obtained by applying a vertex operator to the vertex v_0 . Green nodes indicate qubits that have flipped states, and the red dashed lines encircle nodes considered in the subsequent calculation.

6 Arbitrary ground state of RBM

To further elucidate the analytical solutions derived in the last section, we numerically factorize them on a 3×3 square lattice, as detailed in Appendix C). Setting $(a_j, b_f, w_{f,j}, b_v, w_{v,j}) = (0, 0, \frac{\pi}{4}i, 0, \frac{\pi}{2}i)$ isotropically results in the ground state $|GS\rangle = -|00\rangle + |01\rangle + |10\rangle - |11\rangle$. Conversely, if we change $w_{v,j} = 0, 0, \frac{\pi}{2}i, \frac{\pi}{2}i$ for the respective directions, the ground state becomes $|GS\rangle = +|00\rangle + |01\rangle + |10\rangle + |11\rangle$. Different settings of $w_{v,j}$ can alter the coefficients of the basis states forming the ground state, although these changes are confined to factors of ± 1 . This limitation underscores the representational capacity of the FRRBM. Consequently, it prompts a natural question: how can one prepare an arbitrary ground state?

Inspired by the action of the logical operators Z_v and Z_h , we introduce three additional hidden neurons (h_x , h_y , and h_z) to the FRRBM, enabling it to encapsulate the topological information of ground states in a 2D toric code. These neurons have non-local connections as depicted in Figure 5. We demonstrate that the inclusion of h_x , h_y , and h_z allows for the simulation of any arbitrary ground state. The wave function in Equation (8) is modified as follows:

$$\Psi_M(S; \mathcal{W}) = e^{\sum_j a_j \sigma_j^z} \prod_{e \in \{x,y,z\}} \Gamma_e(S; \mathcal{W}) \prod_{v \in V} \Gamma_v(S; \mathcal{W}) \prod_{f \in F} \Gamma_f(S; \mathcal{W}), \quad (15)$$

$$\Gamma_e(S; \mathcal{W}) = 2 \cosh(b_e + \sum_j w_e \sigma_j^z). \quad (16)$$

If we set the parameters $(a_j, b_f, w_{f,j}, b_v, w_{v,j}, w_{x,y,z})$ to $(0, 0, \frac{\pi}{4}i, 0, \frac{\pi}{2}i, \frac{\pi}{4}i)$, the unnormalized ratio of the ground state on a 3×3 square lattice can be analytically derived:

$$\langle GS|00\rangle = -\cosh(b_x + \frac{\pi}{4}i) \cosh(b_y + \frac{\pi}{4}i) \cosh(b_z + \frac{\pi}{2}i), \quad (17)$$

$$\langle GS|01\rangle = \cosh(b_x - \frac{\pi}{4}i) \cosh(b_y + \frac{\pi}{4}i) \cosh(b_z), \quad (18)$$

$$\langle GS|10\rangle = \cosh(b_x + \frac{\pi}{4}i) \cosh(b_y - \frac{\pi}{4}i) \cosh(b_z), \quad (19)$$

$$\langle GS|11\rangle = -\cosh(b_x - \frac{\pi}{4}i) \cosh(b_y - \frac{\pi}{4}i) \cosh(b_z - \frac{\pi}{2}i). \quad (20)$$

For example, we can select the degeneracy state $|00\rangle$ by setting (b_x, b_y, b_z) to $(\frac{3\pi}{4}i, \frac{3\pi}{4}i, \frac{\pi}{2}i)$. Arbitrary ground states with amplitude ratios like $\langle GS|00\rangle : \langle GS|01\rangle : \langle GS|10\rangle : \langle GS|11\rangle = 1:2:3:4$ can be exactly solved. While an exact solution for certain ratios containing 0 may not exist, we can approximate these by setting the zeros to extremely small values. Further details are provided in Appendix D. While this generalization sacrifices the simplicity of local connections, it remains analytically solvable and enables the simulation of all possible ground states in a clean manner. It also retains the ability to manipulate string operators and has demonstrated both efficient and accurate performance when applied with machine learning techniques.

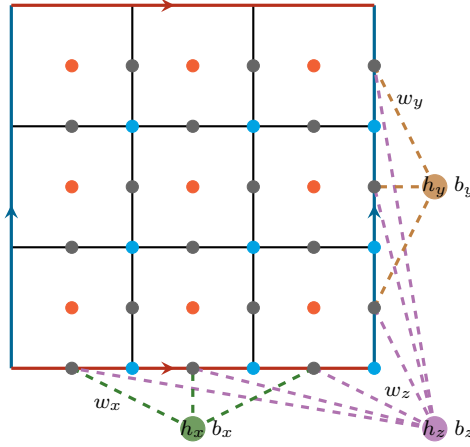


Figure 5: Three hidden neurons (h_x, h_y, h_z) are introduced into the FRRBM to simulate an arbitrary ground state. h_x connects to visible neurons along a horizontal loop, h_y connects along a vertical loop, and h_z connects to all neurons connected by h_x and h_y . Each connection type from a specific hidden neuron is uniformly weighted (w_x, w_y, w_z).

7 Efficiency and Learnability of the RBM

To make $|\Psi\rangle = \sum_S \Psi_M(S; \mathcal{W})|S\rangle$ best represent the ground state $|GS\rangle$, we train the network weights \mathcal{W} in the wave function Ψ_M (as defined in Equation (15)) by optimizing a cost function derived from stabilizer conditions and ground state amplitude ratios. For each configuration S in the selected set \mathcal{S} , we compute the differences in the wave function before and after applying each stabilizer operation⁶. The stabilizer cost function (Equation (21)) is then the total sum of these differences over all selected configurations. Moreover, the cost function for an arbitrary ground state (Equation (22)) includes an additional term accounting for the differences between the modeled amplitudes and the expected amplitudes of the ground state.

$$cost = \sum_{S \in \mathcal{S}} \left(\sum_v |\Psi_M(S) - \Psi_M(A_v S)| + \sum_f |\Psi_M(S) - B_f \Psi_M(S)| \right), \quad (21)$$

$$COST = cost + \lambda \sum_{S \in \mathcal{S}'} |\langle \Psi | S \rangle - \langle GS | S \rangle|, \quad (22)$$

⁶As $|S\rangle$ is a product state, the action of A_v on $|S\rangle$ changes the state, whereas the action of B_f only multiplies it by a number.

where λ is an adjustable parameter and \mathcal{S}' is a subset of configurations used to characterize $|GS\rangle$, as detailed Appendix D.

In prior work [7], the authors analytically derived a solution for the face terms and trained the FRRBM using a vertex stabilizer condition on a portion of a larger square lattice, employing a large number of random configurations. In contrast, our study analytically derives both face and vertex terms and numerically verifies their learnability on square lattices of various sizes using a significantly reduced set of configurations \mathcal{S} . For example, as demonstrated in Figure 6, only 50 configurations—20 selected for the degeneracy basis and 30 random configurations—are required to achieve high precision on a 3×3 square lattice. This approach is both efficient and accurate compared to methods that rely on large numbers of random configurations.

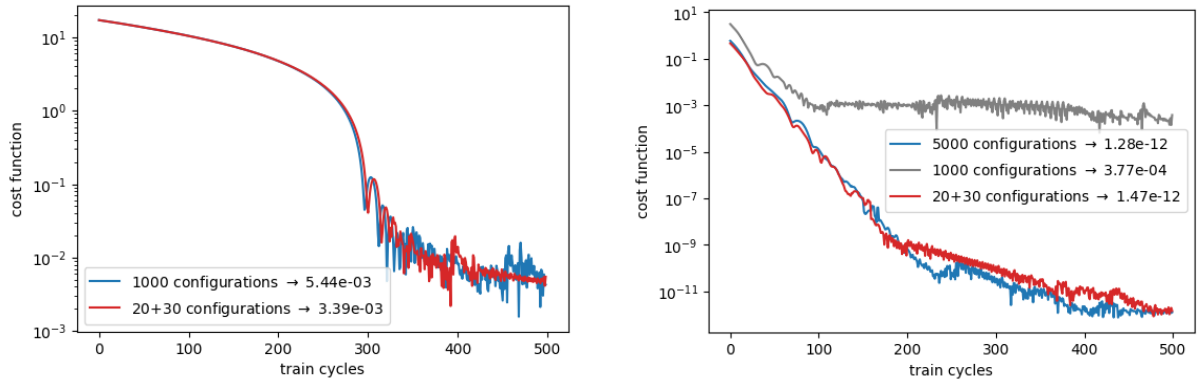


Figure 6: On a 3×3 square lattice, we separately train the face terms and vertex terms using face stabilizer and vertex stabilizer conditions, respectively. The left plot compares the training efficiencies of large number of random configurations and the selected configurations for face terms, while the right plot does the same for vertex terms.

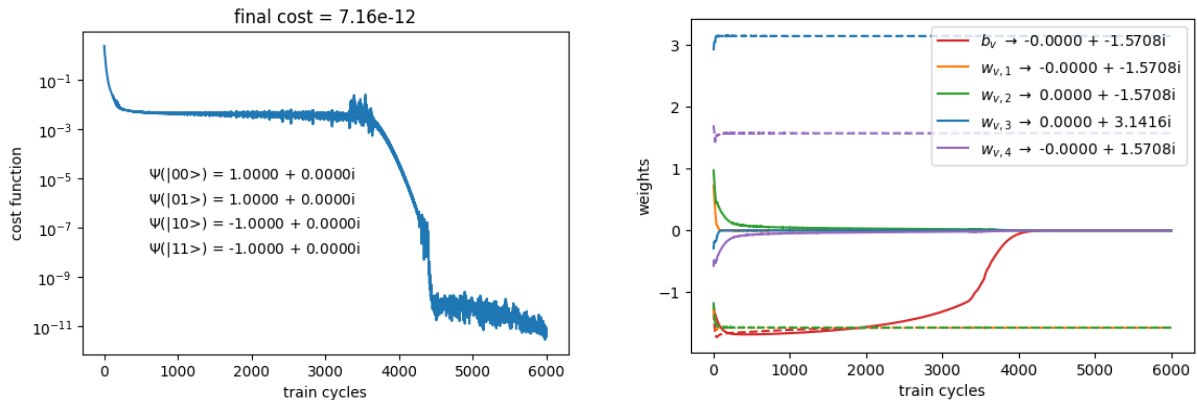


Figure 7: On a 3×3 square lattice, this example demonstrates the existence of barren plateaus, characterized by a sudden drop in performance after prolonged training.

As learnability is influenced by the initial settings, we randomly select 10,000 settings for $b_v \in \mathbb{C}$ and $w_v \in \mathbb{C}$ to numerically search for solutions to the constraints. Despite this extensive search, the presence of *Barren Plateaus*, illustrated in Figure 7, limited us to only 20 solutions. Although the search parameters b_v and w_v were complex, we found solutions only where both b_v and w_v are purely imaginary. Barren plateaus are regions

in the optimization landscape where gradients vanish, impeding any significant learning progress. This phenomenon explains why our search procedure, with limited training time, only yielded a few solutions.

8 Generalization from \mathbb{Z}_2 to \mathbb{Z}_n

In previous sections, we determined the weights of the RBMs analytically and numerically to assess their representational capabilities. Notably, B_f selects configurations with trivial flux that can survive, while A_v ensures that all configurations have uniform weight across a logical state. Among the ground state solutions we found, a ‘trivial solution’ with $(b_f, w_{f,j}, b_v, w_{v,j}) = (0, \frac{\pi}{4}i, 0, 0)$ emerged, where each survived configuration possess equal weight. We observe that ignoring vertex-type hidden neurons in the FRRBM still provides a good solution. When B_f selects survival configurations, it assigns each configuration an equal weight, thereby automatically fulfilling the action of A_v . This observation receives ancillary support from the work [8], where an FRRBM was constructed without using face-type hidden neurons, equivalent to our approach when aligned with our notation. This idea can be generalized to implement the *Kitaev quantum double model* associated with the group Z_N ⁷. The model, set on an oriented lattice with a $|G|$ -dimensional qudit on each edge labeled by a group element g , follows the convention in [16]. Though the Hamiltonian resembles Equation (1), A_v and B_f are defined in a different manner. As shown in Figure 8, we focus exclusively on the action of B_f :

$$B_f|v_1 v_2 v_3 v_4\rangle = \delta_{p_g, 1_g}|v_1 v_2 v_3 v_4\rangle, \quad (23)$$

where 1_g is the identity element of the group G , and p_g is the group product of states on each edge bordering the face counterclockwise⁸. If an edge’s direction aligns with the orientation, we include v_i ; otherwise, we use v_i^{-1} . Thus, $p_g = \prod_i v_i^{a_i}$, where $a_i = \pm 1$ reflects this alignment. Specifically, for $G = Z_N$, the state of the N -dimensional qudit is labelled by $0, 1, \dots, N-1$. In this setting, the group product is arithmetic summation, the identity element 1_g is 0, and each element is its own inverse. Then the action of B_f is significantly simplified:

$$B_f|v_1 v_2 v_3 v_4\rangle = \delta_{\sum_i v_i, 0}|v_1 v_2 v_3 v_4\rangle. \quad (24)$$

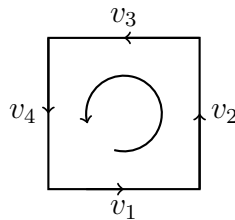


Figure 8: Convention for the local operator: Edges are ordered counterclockwise as v_1, v_2, v_3, v_4 , with directions indicated by arrows on each edge.

⁷For $N = 2$, the model corresponds to the toric code with a basis change to match notation in previous sections.

⁸We need to pick up a start-up vertex, though it turns out to be insignificant.

We utilize a natural RBM to implement the above action, corresponding to the condition $\sum v_i = 0 \pmod{N}$. This is achieved using an N -dimensional invisible qudit u with the setting of isotropic weights $(b, w_i) = (0, \frac{2\pi i}{N})$:

$$\sum_{u=0}^{N-1} \exp(b + \sum_i uw_i v_i) = \frac{1 - \exp(2\pi i(b + \sum_i v_i))}{1 - \exp(2\pi i(b + \sum_i v_i)/N)} = \begin{cases} N & \text{if } b + \sum_i v_i = 0 \pmod{N}, \\ 0 & \text{otherwise.} \end{cases} \quad (25)$$

The action of A_v is safely neglected here, as the RBM already simulates a ground state that is an equal superposition of all logical bases. And this expression explicitly ensures the flux-free requirement. A complete basis of the ground state can be found in the same manner as illustrated in Figure 5. It offers a natural method for creating fluxions by setting $b \neq 0$, though such creation is not arbitrary on a closed manifold due to global constraints. They are elementary magnetic excitations, since each element of Z_N represents a unique conjugacy class. We show generalized X and Z operators as follows:

$$X = \begin{pmatrix} 0 & 1 & 0 & \cdots & 0 \\ 0 & 0 & 1 & \cdots & 0 \\ 0 & 0 & 0 & \cdots & 0 \\ \vdots & \vdots & \vdots & \ddots & \vdots \\ 1 & 0 & 0 & \cdots & 0 \end{pmatrix}, \quad Z = \begin{pmatrix} 1 & 0 & 0 & \cdots & 0 \\ 0 & \omega & 0 & \cdots & 0 \\ 0 & 0 & \omega^2 & \cdots & 0 \\ \vdots & \vdots & \vdots & \ddots & \vdots \\ 0 & 0 & 0 & \cdots & \omega^{n-1} \end{pmatrix}, \quad (26)$$

where $\omega = e^{2\pi i/N}$ is the N -th root of unity. Generalized X substitutes the value of a visible node v_i by $v_i + 1$, utilizing the RBM's action which operates modulo N . Generalized Z is implemented by adding a magnetic coupling $a = 2\pi i/N$ to the visible node. By applying these string operators composed of the generalized X and Z , all excitations can be created on our RBM.

This method can be generalized to other lattice models with frustration-free Hamiltonians composed of two types of terms: one type is the tensor product of only Pauli-Z matrices, which constrain local flux, and the other is the tensor product of only Pauli-X matrices, which enable gauge transformations, as in all CSS codes. Applying the flux-free RBM achieves an equal superposition of all flux-free configurations, automatically satisfying the gauge transformation terms and resulting in a superposition of all logical states. For instance, this approach is applicable to the X-cube model, the checkerboard model, Haah codes, the Kitaev model associated with Abelian groups, and so on. However, the generalization to the Kitaev quantum double model associated with a non-Abelian group remains unclear.

9 Conclusion and further work

We analytically resolved the FRRBM proposed for the toric code, determining all possible ground states to assess the model's capabilities. We then modified this model to support arbitrary ground states through the integration of non-local connections. This enhanced model remains analytically solvable and can also be efficiently solved using machine learning techniques. We then extend our work to Kitaev quantum double model associated with abelian group Z_N . Our ongoing research aims to investigate feasible RBM implementations for more specific codes, including those for the Double Semion [17], Fibonacci Anyon [17, 18], and Kitaev quantum double model associated with a non-abelian group.

Acknowledgement. The authors are partially supported by NSF grant CCF-2006667, Quantum Science Center sponsored by DOE’s Office of Science, and ARO MURI.

References

- [1] A Yu Kitaev. Fault-tolerant quantum computation by anyons. *Annals of Physics*, 303(1):2–30, 2003.
- [2] Michael H Freedman, Michael Larsen, and Zhenghan Wang. A modular functor which is universal for quantum computation. *Communications in Mathematical Physics*, 227(3):605–622, 2002.
- [3] Tobias J Osborne. Hamiltonian complexity. *Reports on progress in physics*, 75(2):022001, 2012.
- [4] Geoffrey E Hinton, Simon Osindero, and Yee-Whye Teh. A fast learning algorithm for deep belief nets. *Neural computation*, 18(7):1527–1554, 2006.
- [5] Giuseppe Carleo and Matthias Troyer. Solving the quantum many-body problem with artificial neural networks. *Science*, 355(6325):602–606, 2017.
- [6] Dong-Ling Deng, Xiaopeng Li, and S Das Sarma. Quantum entanglement in neural network states. *Physical Review X*, 7(2):021021, 2017.
- [7] Dong-Ling Deng, Xiaopeng Li, and S Das Sarma. Machine learning topological states. *Physical Review B*, 96(19):195145, 2017.
- [8] Jing Chen, Song Cheng, Haidong Xie, Lei Wang, and Tao Xiang. Equivalence of restricted boltzmann machines and tensor network states. *Physical Review B*, 97(8):085104, 2018.
- [9] Xun Gao and Lu-Ming Duan. Efficient representation of quantum many-body states with deep neural networks. *Nature communications*, 8(1):662, 2017.
- [10] Sirui Lu, Xun Gao, and L-M Duan. Efficient representation of topologically ordered states with restricted boltzmann machines. *Physical Review B*, 99(15):155136, 2019.
- [11] Zhih-Ahn Jia, Yuan-Hang Zhang, Yu-Chun Wu, Liang Kong, Guang-Can Guo, and Guo-Ping Guo. Efficient machine-learning representations of a surface code with boundaries, defects, domain walls, and twists. *Physical Review A*, 99(1):012307, 2019.
- [12] Maarten Van den Nest, Jeroen Dehaene, and Bart De Moor. Graphical description of the action of local clifford transformations on graph states. *Physical Review A*, 69(2):022316, 2004.
- [13] Nicolas Le Roux and Yoshua Bengio. Representational power of restricted boltzmann machines and deep belief networks. *Neural computation*, 20(6):1631–1649, 2008.
- [14] Yichen Huang, Joel E Moore, et al. Neural network representation of tensor network and chiral states. *Physical Review Letters*, 127(17):170601, 2021.

- [15] Pengcheng Liao and David L Feder. Graph-state representation of the toric code. *Physical Review A*, 104(1):012432, 2021.
- [16] Bowen Yan, Penghua Chen, and Shawn X Cui. Ribbon operators in the generalized kitaev quantum double model based on hopf algebras. *Journal of Physics A: Mathematical and Theoretical*, 55(18):185201, 2022.
- [17] Michael A Levin and Xiao-Gang Wen. String-net condensation: A physical mechanism for topological phases. *Physical Review B*, 71(4):045110, 2005.
- [18] Chien-Hung Lin, Michael Levin, and Fiona J Burnell. Generalized string-net models: A thorough exposition. *Physical Review B*, 103(19):195155, 2021.

A Analytical solution of $b_f, w_{f,j}$ in the FRRBM

To optimize $|\Psi\rangle = \sum_S \Psi_M(S; \mathcal{W})|S\rangle$ to best represent the ground state $|GS\rangle$, consider the following expression:

$$\Psi_M(S; \mathcal{W}) = e^{\sum_j a_j \sigma_j^z} \prod_{v \in V} \Gamma_v(S; \mathcal{W}) \prod_{f \in F} \Gamma_f(S; \mathcal{W}), \quad (27)$$

$$\Gamma_v(S; \mathcal{W}) = 2 \cosh(b_v + \sum_{j \in s(v)} w_{v,j} \sigma_j^z), \quad (28)$$

$$\Gamma_f(S; \mathcal{W}) = 2 \cosh(b_f + \sum_{j \in s(f)} w_{f,j} \sigma_j^z). \quad (29)$$

Setting $a_j = 0$, we treat $|\Psi\rangle$ as $|GS\rangle$:

$$\begin{aligned} |GS\rangle &= \sum_S e^{\sum_j a_j \sigma_j^z} \prod_{v \in V} 2 \cosh(b_v + \sum_{j \in s(v)} w_{v,j} \sigma_j^z) \\ &\quad \prod_{f \in F} 2 \cosh(b_f + \sum_{j \in s(f)} w_{f,j} \sigma_j^z) |S\rangle. \end{aligned} \quad (30)$$

The stabilizer condition of face operator is examined next:

$$B_f |GS\rangle = \prod_{e \in s(f)} \hat{\sigma}_e^z |GS\rangle = |GS\rangle, \forall f. \quad (31)$$

As the configuration $|S\rangle$ remains unchanged by $\hat{\sigma}_e^z$, we get:

$$\begin{aligned} &\prod_{e \in s(f)} \hat{\sigma}_e^z e^{\sum_j a_j \sigma_j^z} \prod_{v \in V} \Gamma_v(S; \mathcal{W}) \prod_{f' \in F} \Gamma_{f'}(S; \mathcal{W}) \\ &= e^{\sum_j a_j \sigma_j^z} \prod_{v \in V} \Gamma_v(S; \mathcal{W}) \prod_{f' \in F} \Gamma_{f'}(S; \mathcal{W}), \forall f, \forall S. \end{aligned} \quad (32)$$

All irrelevant terms on both sides are then cancelled:

$$\prod_{e \in s(f)} \hat{\sigma}_e^z \cosh(b_f + \sum_{j \in s(f)} w_{f,j} \sigma_j^z) = \cosh(b_f + \sum_{j \in s(f)} w_{f,j} \sigma_j^z), \forall f, \forall S. \quad (33)$$

Due to translation invariance, it is unnecessary to repeat the calculation for all faces. Instead, the possible configurations in a single face contribute 2^4 equations, as illustrated in Figure 9:

$$\cosh(b - w_1 + w_2 + w_3 + w_4) = 0 \quad (34)$$

$$\cosh(b + w_1 - w_2 - w_3 - w_4) = 0 \quad (35)$$

$$\cosh(b - w_1 - w_2 + w_3 + w_4) \neq 0 \quad (36)$$

$$\cosh(b - w_1 - w_2 - w_3 - w_4) \neq 0 \quad (37)$$

⋮

Solving these equations yields the complete set of solutions for the face terms $b_f, w_{f,j}$: $b_f = 0 \pmod{\pi}$ and $w_{f,j} = \frac{\pi}{4}i, \frac{3\pi}{4}i \pmod{\pi}$, where an even number of the four $w_{f,j}$ must be the same. Since the function of the face terms selectively excludes some configurations, any solution set is valid and can be chosen without loss of generality. In the main article, we choose the isotropic solution $(b_f, w_{f,j}) = (0, \frac{\pi}{4}i)$.

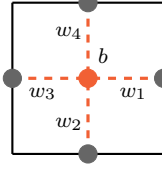


Figure 9: This lattice diagram represents a translation-invariant structure for a face-type hidden neuron, using simplified notation without the subscript f .

B Analytical solution of $b_v, w_{v,j}$ in the FRRBM

The face terms B_f typically rule out certain configurations without trivial flux, while the vertex terms A_v ensures all configurations in the same logical state are uniformly weighted, as illustrated in Figure 10. In this appendix, we continue from Equation (14) discussed in the main article, focusing on the configurations with trivial flux illustrated in Figures 11 through 15. We extract relevant independent equations (39) through (42) to analytically solve for b_v and $w_{v,j}$. To simplify notation further in the calculation, we replace \cosh with \cos and divide all weights by i . We treat b_v as a redundant parameter, similar to a_j , and set $b_v = 0$, as allowing $b_v \in \mathbb{C}$ would introduce superfluous freedom. Further elaboration on this issue is provided at the end.

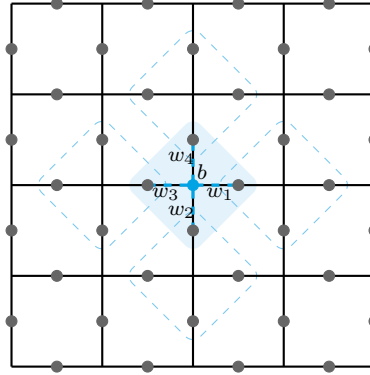


Figure 10: This lattice diagram represents a translation-invariant structure for a vertex-type hidden neuron, using simplified notation without the subscript v and $(b_v, w_{v,j}) = i * (b, w_j)$. If we flip the four qubits surrounding the central vertex, qubits contributing to the phase difference are circled for clarity.

Equation (38) defines the often-used phase factor A :

$$\cos(w_1 + w_2 + w_3 + w_4) := A. \quad (38)$$

Equation (39), the most discussed criterion, is abstracted from Figure 11:

$$\begin{aligned} & \cos(-w_1 + w_2 + w_3 + w_4) \cos(w_1 - w_2 + w_3 + w_4) \\ & \cos(w_1 + w_2 - w_3 + w_4) \cos(w_1 + w_2 + w_3 - w_4) = A^4. \end{aligned} \quad (39)$$

Equations (40, 41, 42) describe squared conditions, while Equations (43, 44) specify additional criteria. All these equations are derived from the configurations shown in

Figure 12 through 15:

$$\begin{aligned} & [\cos(-w_1 - w_2 + w_3 + w_4) \cos(w_1 + w_2 - w_3 - w_4)]^L = A^{2L} \text{ for any } L \\ & \Rightarrow \cos^2(-w_1 - w_2 + w_3 + w_4) = A^2. \end{aligned} \quad (40)$$

$$\begin{aligned} & [\cos(-w_1 + w_2 + w_3 - w_4) \cos(w_1 - w_2 - w_3 + w_4)]^L = A^{2L} \text{ for any } L \\ & \Rightarrow \cos^2(w_1 - w_2 - w_3 + w_4) = A^2. \end{aligned} \quad (41)$$

$$\begin{aligned} & \cos(-w_1 + w_2 - w_3 + w_4) \cos(-w_1 + w_2 + w_3 + w_4) \cos(w_1 + w_2 - w_3 + w_4) = A^3 \\ & \cos(w_1 - w_2 + w_3 - w_4) \cos(w_1 - w_2 + w_3 + w_4) \cos(w_1 + w_2 + w_3 - w_4) = A^3 \\ & \Rightarrow \cos^2(w_1 - w_2 + w_3 - w_4) = A^2. \end{aligned} \quad (42)$$

$$\Rightarrow \cos^2(w_1 - w_2 + w_3 + w_4) \cos^2(w_1 + w_2 + w_3 - w_4) = A^4. \quad (43)$$

$$\Rightarrow \cos^2(-w_1 + w_2 + w_3 + w_4) \cos^2(w_1 + w_2 - w_3 + w_4) = A^4. \quad (44)$$

Next, we need to solve and discuss Equations (38) through (44):

$$\text{Equation (38)+(40): } w_1 + w_2 = 0 \text{ or } w_3 + w_4 = 0$$

$$\text{Equation (38)+(41): } w_1 + w_4 = 0 \text{ or } w_2 + w_3 = 0$$

$$\text{Equation (38)+(42): } w_1 + w_3 = 0 \text{ or } w_2 + w_4 = 0$$

$$\Rightarrow -w_1 = w_2 = w_3 = w_4 \pmod{\frac{\pi}{2}} \text{ and alternations.} \quad (45)$$

$$\text{or } w_1 = w_2 = w_3 = 0 \text{ or } \frac{\pi}{4} \pmod{\frac{\pi}{2}} \text{ and alternations.} \quad (46)$$

In the first scenario derived in Equation (45), without loss of generality, we can set $w_1 = -w + \frac{\pi}{2}m_1$, $w_2 = w + \frac{\pi}{2}m_2$, $w_3 = w + \frac{\pi}{2}m_3$, and $w_4 = w + \frac{\pi}{2}m_4$, where $m_1, m_2, m_3, m_4 \in \mathbb{N}$. Subsequently, the criteria in Equation (39) is rewritten as

$$\begin{aligned} & \cos[4w + \frac{\pi}{2}(M - 2m_1)] \cos[\frac{\pi}{2}(M - 2m_2)] \\ & \cos[\frac{\pi}{2}(M - 2m_3)] \cos[\frac{\pi}{2}(M - 2m_4)] = \cos^4(2w + \frac{\pi}{2}M), \end{aligned} \quad (47)$$

where $M := m_1 + m_2 + m_3 + m_4$. And $\cos[\frac{\pi}{2}(M - 2m_2)] \neq 0 \Rightarrow M$ is even, thus the terms with $\frac{\pi}{2}$ above could be rearranged as follows:

$$\begin{aligned} \cos[4w + \frac{\pi}{2}(M - 2m_1)] &= \cos(4w) \cos\left[\frac{\pi}{2}(M - 2m_1)\right] - \sin(4w) \sin\left[\frac{\pi}{2}(M - 2m_1)\right] \\ &= \cos(4w) \cos\left[\frac{\pi}{2}(M - 2m_1)\right], \end{aligned}$$

or vice versa:

$$\cos[\frac{\pi}{2}(M - 2m_2)] \cos[\frac{\pi}{2}(M - 2m_3)] = \cos[\frac{\pi}{2}(2M - 2m_2 - 2m_3)].$$

Then Equation (47) is simplified as

$$\begin{aligned} \cos(4w) \cos\left[\frac{\pi}{2}(4M - 2M)\right] &= [\cos(2w) \cos(\frac{\pi}{2}M)]^4 \\ \cos(4w) &= \cos^4(2w). \end{aligned} \quad (48)$$

Solving Equation (48), we get $\cos(4w) = 1$, implying $w = 0 \pmod{\frac{\pi}{2}}$. Considering the definition of A in Equation (38), which is not 0, we conclude: **even number of w are $0 \pmod{\pi}$ and the others are $\frac{\pi}{2} \pmod{\pi}$. For these solutions, A is either +1 or -1.**

In the second scenario derived in Equation (46), without loss of generality, we can set $w_1 = w_2 = w_3 = w$, $w = 0$ or $\frac{\pi}{4} \pmod{\frac{\pi}{2}}$ and w_4 is free. By inserting all possible values of w_1, w_2 and w_3 into Equations (39) and (43, 44), we can find the allowed solutions: **three of w equal to $0 \pmod{\frac{\pi}{2}}$ and the other serves as a normalization parameter such that $\cos(3w + w_4) = A$.**

In the calculation above, we treat b as a redundant parameter and set $b = 0$. Reader can practice by setting $b = \frac{\pi}{2}$ to obtain another set of solutions, which yields results similar to those above. To understand how allowing $b \in \mathbb{C}$ introduces superfluous freedom, one can abstract Equation (49) from Figure 16 and incorporate b into Equation (38). By re-deriving Equations (39) through (42) and substituting them into Equation (49), one can obtain Equation (50), which represents the restriction on b . There are infinite many possibilities, and above two learnable solutions emerge through the training process introduced in the next section.

$$\begin{aligned} & \cos(b - w_1 - w_2 + w_3 + w_4) \cos(b + w_1 - w_2 - w_3 + w_4) \cos(b + w_1 + w_2 - w_3 - w_4) \\ & \cos(b - w_1 + w_2 + w_3 - w_4) \cos^2(b + w_1 - w_2 - w_3 - w_4) \cos^2(b - w_1 + w_2 - w_3 - w_4) \\ & \cos^2(b - w_1 - w_2 + w_3 - w_4) \cos^2(b - w_1 - w_2 - w_3 + w_4) = A^{12}. \end{aligned} \quad (49)$$

$$\cos^4(b - w_1 - w_2 - w_3 - w_4) = \cos^4(b + w_1 + w_2 + w_3 + w_4). \quad (50)$$

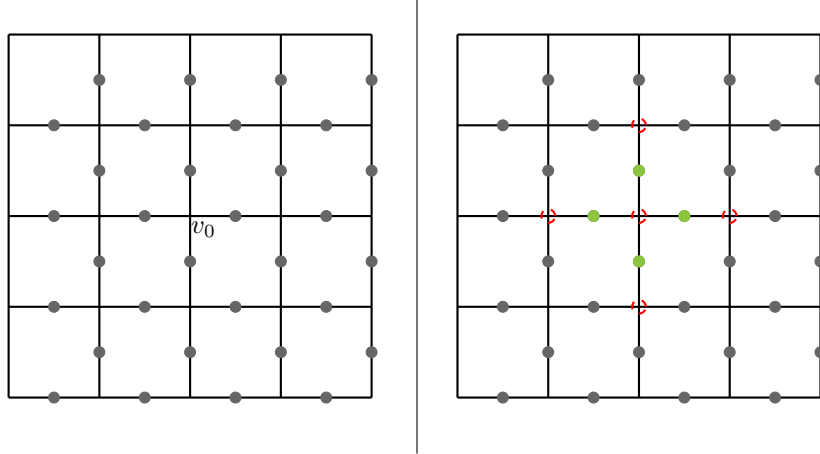


Figure 11: In this configuration, each black dot represents a qubit in state $| -1 \rangle$, while each green dot indicates a qubit in state $| +1 \rangle$. Starting with the initial configuration on the left, a vertex operator is applied at vertex v_0 to flip the adjacent four qubits. The resulting configuration, displayed on the right, features five vertices encircled in red that contribute to the phase difference. By comparing the phase contributions from these vertices in both configurations, we derive Equation (39), which is a crucial criterion for our calculation.

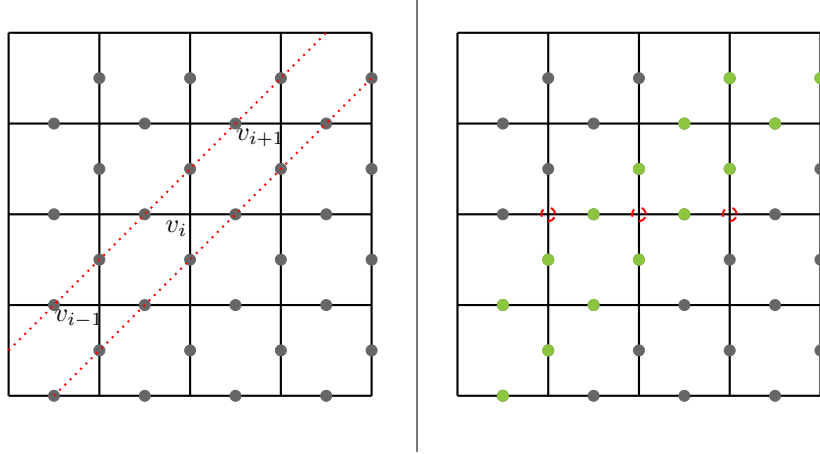


Figure 12: Starting with the initial configuration illustrated on the left, we apply vertex operators diagonally at vertices v_0 . The resultant configuration, showcased on the right, exhibits translational symmetry horizontally. Notably, the three vertices encircled in red contribute to the phase difference. By analyzing the phase contributions from these three vertices in both configurations, we deduce Equation (40). This equation represents one of the three pivotal square conditions essential for our calculation.

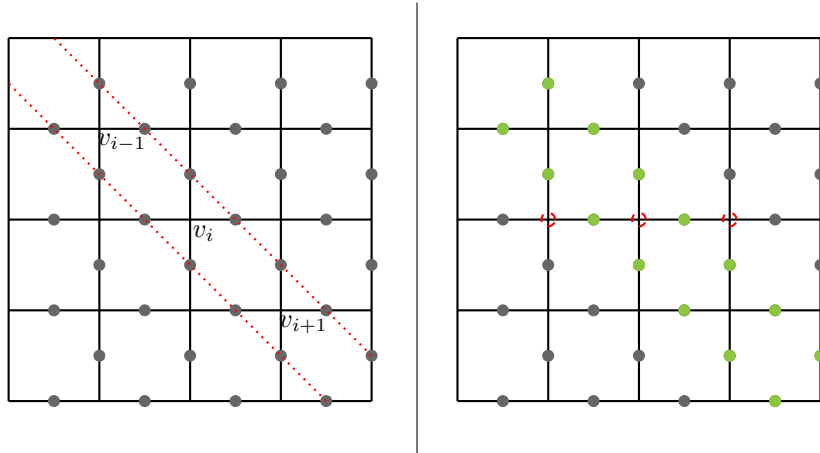


Figure 13: Similarly, applying vertex operators diagonally in the perpendicular direction, we obtain Equation (41), another pivotal square condition.

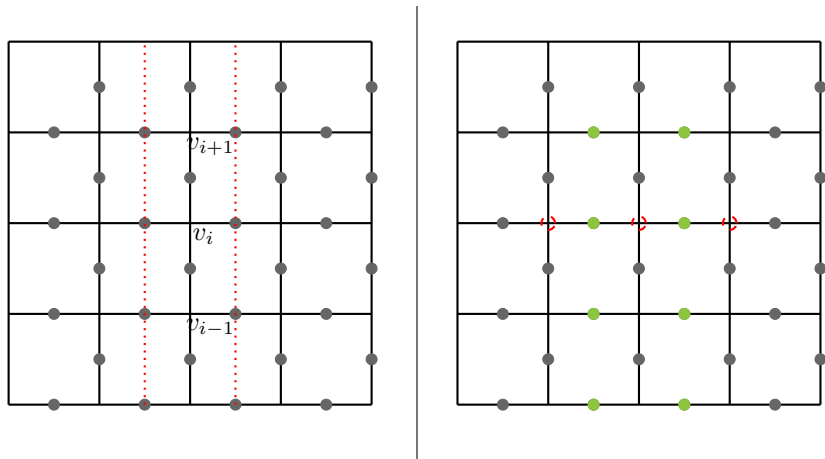


Figure 14: This configuration corresponds to the first equation to derive the Equation (42), the last pivotal square condition.

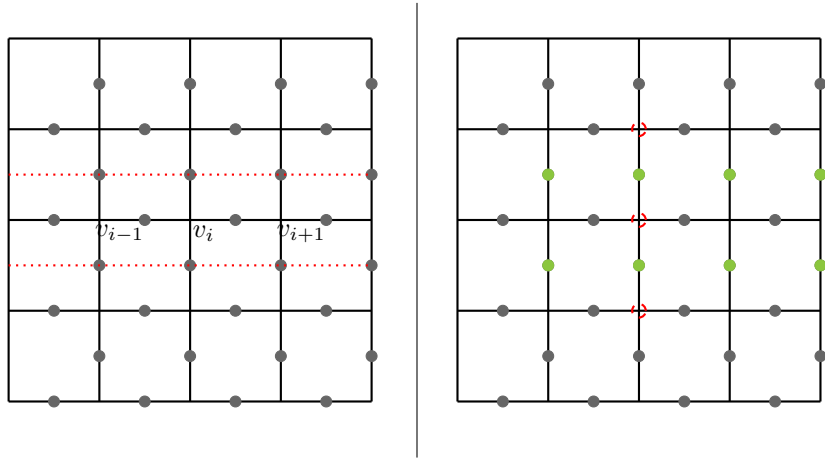


Figure 15: This configuration corresponds to the second equation to derive the Equation (42), the last pivotal square condition.

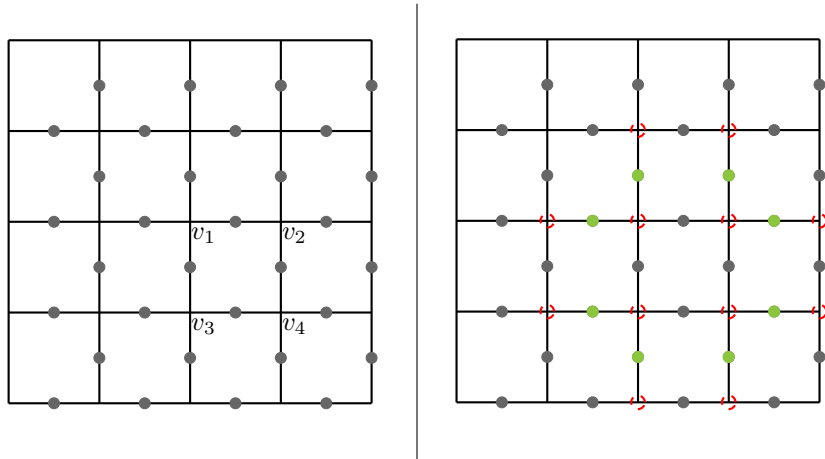


Figure 16: This configuration corresponds to Equation (49), the condition to find the restriction on b_v .

C Machine Learning of the FRRBM

To further elucidate the analytical solutions derived in the main article for the FRRBM illustrated in Figure 3, we numerically determine the ground state solution from Equations (6) and (8) by applying a vertex stabilizer condition on square lattices of various sizes. Namely, Figures 17, 18 and 19 show their factorization on 3×3 , 4×4 and 5×5 square lattices with different initial settings, where the common setting is $(a_j, b_f, w_{f,j}, b_v) = (0, 0, \frac{\pi}{4}i, 0)$, with variations in $w_{v,j}$ making the difference.

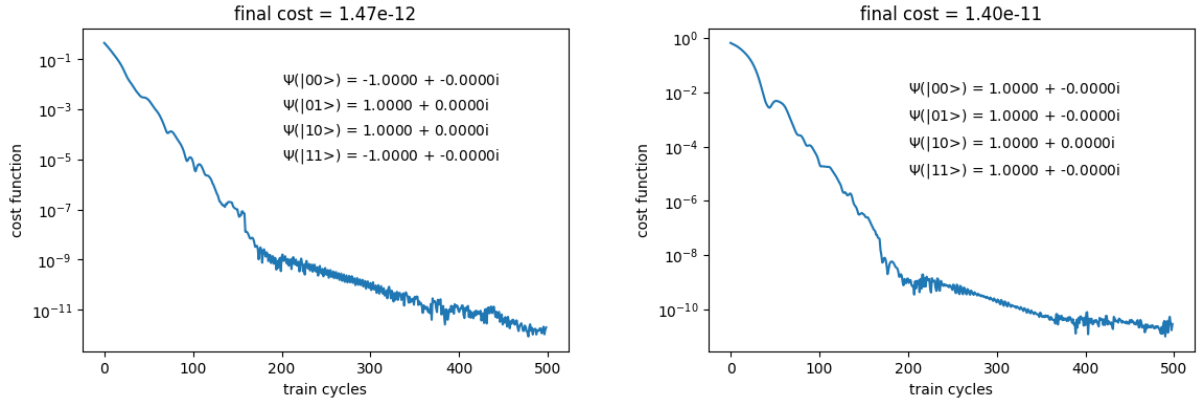


Figure 17: On a 3×3 lattice, the left plot shows the training result for the isotropic setting $w_{v,j} = \frac{\pi}{2}i$, and right for the anisotropic setting $w_{v,j} = 0, 0, \frac{\pi}{2}i, \frac{\pi}{2}i$.

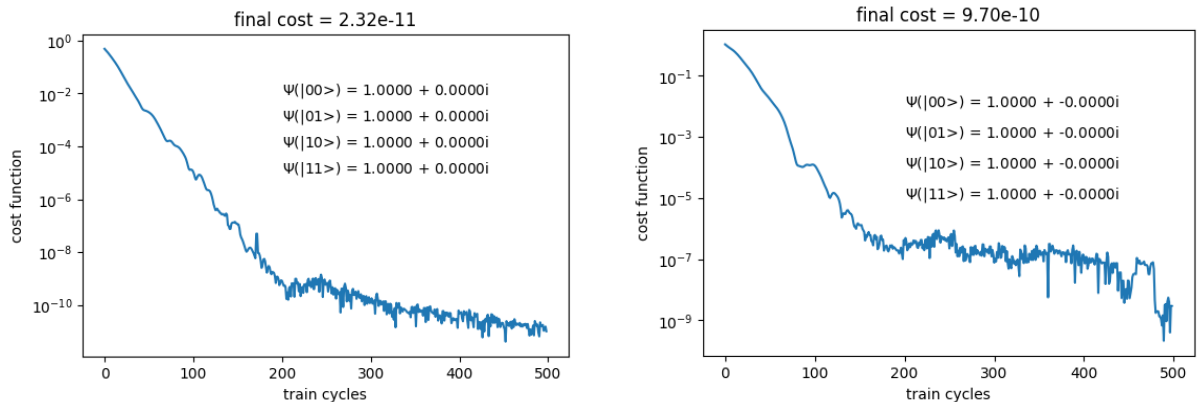


Figure 18: On a 4×4 lattice, the left plot shows the training result for the isotropic setting $w_{v,j} = \frac{\pi}{2}i$, and right for the anisotropic setting $w_{v,j} = 0, 0, \frac{\pi}{2}i, \frac{\pi}{2}i$. Despite the varied interaction settings, both configurations yield identical ground states. This outcome contrasts with the results shown in Figure 17, where the ground states differ significantly.

As the system size increases, achieving the same level of precision necessitates a corresponding increase in the number of selected configurations. For example, in the plots shown above, the numbers of selected configurations are 50, 100, and 150 for progressively larger systems. Consequently, the training time and computational resources required increase proportionally with the system size. This escalation represents a common challenge when optimizing parameters in neural network representations of quantum states.

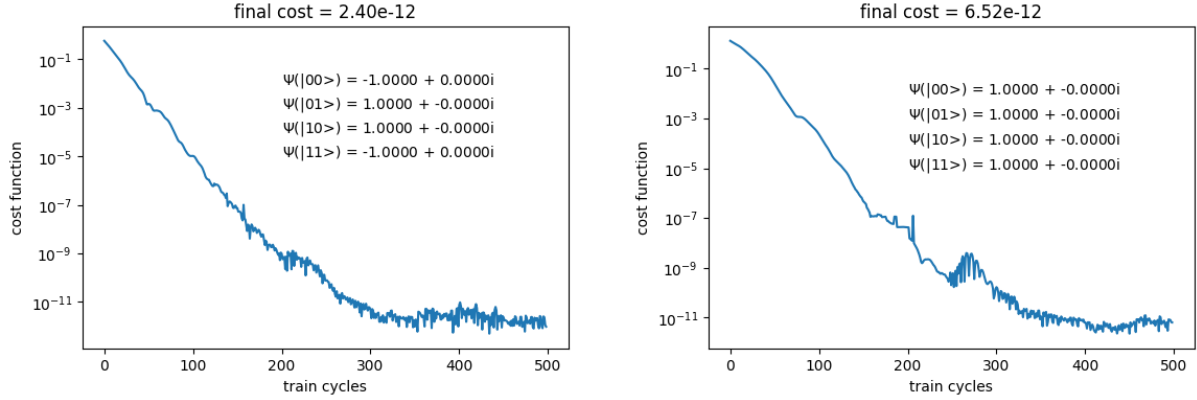


Figure 19: On a 5×5 lattice, the left plot shows the training result for the isotropic setting $w_{v,j} = \frac{\pi}{2}i$, and right for the anisotropic setting $w_{v,j} = 0, 0, \frac{\pi}{2}i, \frac{\pi}{2}i$. This outcome align with the results shown in Figure 17.

D Machine Learning of the RBM

Illustrated in Figure 5, we pick the isotropic setting $(a_j, b_f, w_{f,j}, b_v, w_{v,j}) = (0, 0, \frac{\pi}{4}i, 0, \frac{\pi}{2}i)$ and uniformly weighted every new connection ($w_{x,y,z} = \frac{\pi}{4}i$). Then three hidden neurons (h_x , h_y , h_z) are introduced into the FRRBM to simulate an arbitrary ground state. Reader can verify that the inclusion of h_x and h_y (inspired by the logical operators Z_v and Z_h) allows for the simulation of any specific degeneracy state, while h_z enables the representation of any arbitrary ground state as a linear combination within the degeneracy basis. Then, using Equations from (17) to (20), we can analytically solve the weights for arbitrary ground state.

On the other hand, illustrated in Figure 20, the set of selected configurations $\mathcal{S}' = \{S_1, S_2, S_3, S_4\}$ are chosen from the equi-positioned configurations of the states $|00\rangle$, $|01\rangle$, $|10\rangle$, $|11\rangle$, respectively. Employing the condition $\langle GS|S1\rangle : \langle GS|S2\rangle : \langle GS|S3\rangle : \langle GS|S4\rangle = \langle GS|00\rangle : \langle GS|01\rangle : \langle GS|10\rangle : \langle GS|11\rangle$, we can numerically train the weights for arbitrary ground state according to the ratio conditions.

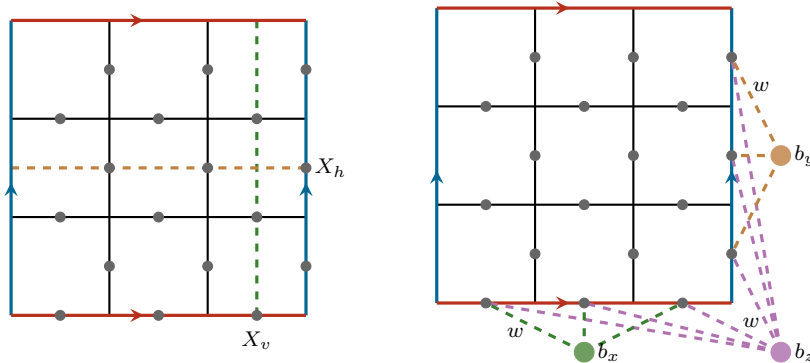


Figure 20: On the square lattice displayed on the left, we identify four distinct qubit configurations: S_1 , where all qubits are in the $| -1 \rangle$ state; S_2 , with qubits only on the vertical dashed loop in the $| 1 \rangle$ state, namely $|S_2\rangle = X_v|S1\rangle$; similarly $|S_3\rangle = X_h|S1\rangle$; and $|S_4\rangle = X_hX_v|S1\rangle$. The weights of interest are illustrated on the right.

Let us consider a straightforward example involving the degeneracy state $|00\rangle$. We employ the condition $\langle GS|S1\rangle : \langle GS|S2\rangle : \langle GS|S3\rangle : \langle GS|S4\rangle = 1 : 0 : 0 : 0$ to analytically

determine the weights, yielding in $(b_x, b_y, b_z) = (\frac{3\pi}{4}i, \frac{3\pi}{4}i, \frac{\pi}{2}i)$. Subsequently, we verify the learnability of the RBM, as illustrated in Figure 21, ensuring that it can accurately and efficiently represent the specified state characteristics.

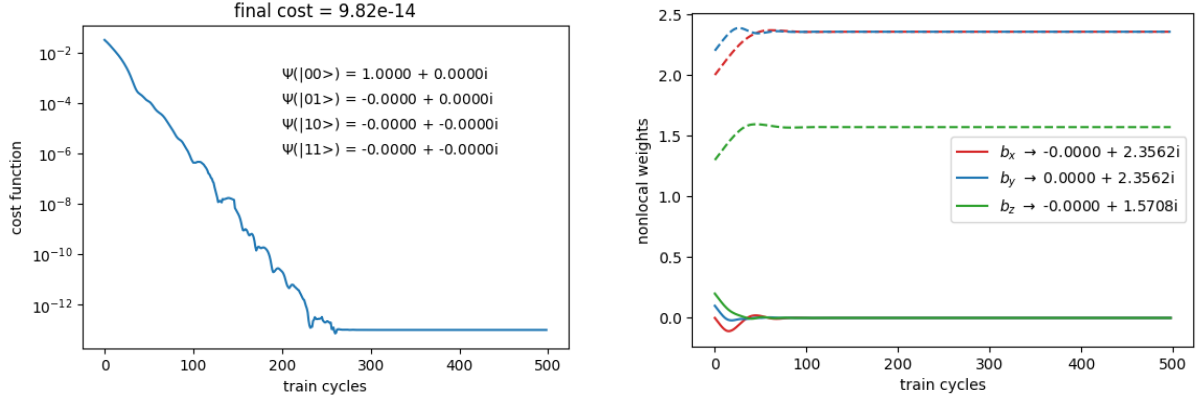


Figure 21: Training results on a 3×3 lattice for $|GS\rangle = |00\rangle$.

Similarly, another example with amplitude ratios $\langle GS|00\rangle : \langle GS|01\rangle : \langle GS|10\rangle : \langle GS|11\rangle = 1 : 2 : 3 : 4$ results in the solution $(b_x, b_y, b_z) = (\coth^{-1}(2\sqrt{2/3}) + \frac{\pi}{4}i, \coth^{-1}(\sqrt{6}) + \frac{\pi}{4}i, \coth^{-1}(\sqrt{3/2}))$. We then verify the learnability of the RBM, as illustrated in Figure 22. We find that finer results can be achieved with smaller training step sizes, though extending training time does not lead to significant improvements. Finally, we present an example that can only be approximated, as shown in Figure 23. We observe that finer results are achievable with smaller training step sizes, and unlike the previous case, longer training times also contribute to better outcomes.

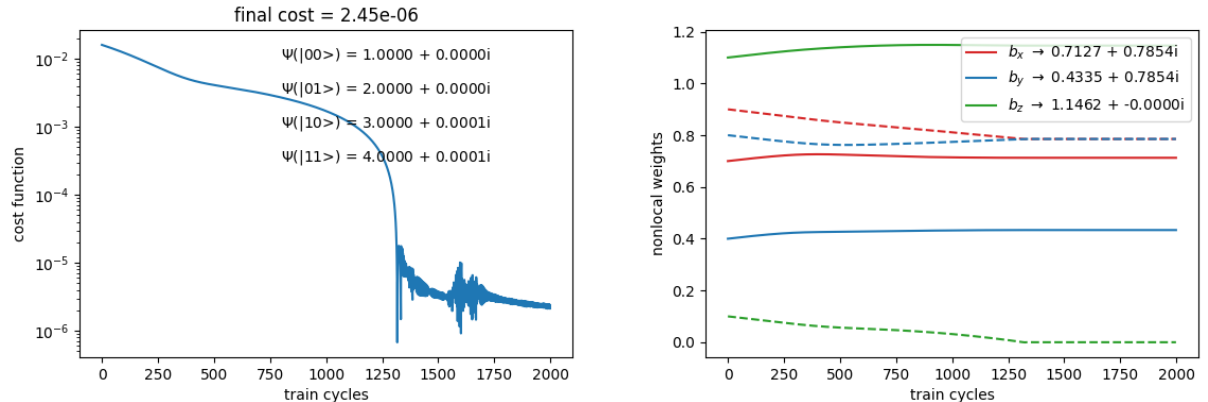


Figure 22: Training results on a 3×3 lattice for $|GS\rangle = |00\rangle + 2|01\rangle + 3|10\rangle + 4|11\rangle$.

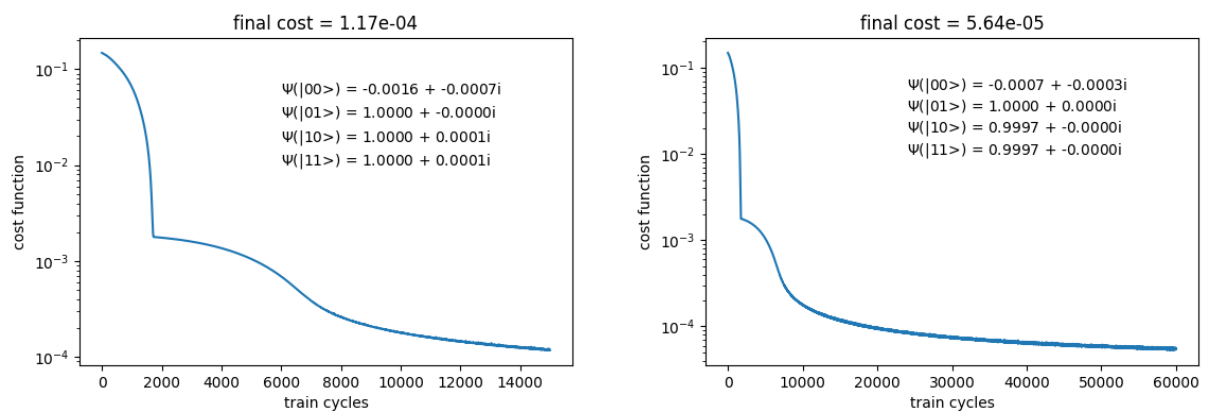


Figure 23: Training results on a 3×3 lattice for $|GS\rangle = |01\rangle + |10\rangle + |11\rangle$.